J. Fluid Mech. (1990), *vol.* 219, *pp.* 51–80
Printed in Great Britain

Experiments on ripple instabilities. Part 2 Selective amplification of resonant triads

By MARC PERLIN†, DIANE HENDERSON‡ AND JOE HAMMACK

Department of Aerospace Engineering, Mechanics & Engineering Sciences, University of Florida, Gainesville, FI 32611 USA

(Received 7 August 1989)

Resonant three-wave interactions among capillary–gravity water waves are studied experimentally using a test wavetrain and smaller background waves (noise) generated mechanically in a channel. The spectrum of the background waves is varied from broad-banded to one with discrete components. When the noise spectrum is broad-banded, the test wavetrain amplifies all waves in its low-frequency band of allowable triads B_ℓ, as anticipated from RIT (resonant interaction theory). When the noise spectrum has a discrete component in the high-frequency band of allowable triads B_h, the test wavetrain selectively amplifies a triad with two waves from B_ℓ, contrary to expectations based on RIT. (Although, in accordance with RIT, no waves in B_h are amplified.) We conjecture that the mechanism for selective amplification comprises a sequence of exceedingly weak, higher-order interactions, normally neglected in RIT. This sequence allows the small amount of energy in a discrete spectral component to cascade to two waves in B_ℓ, which then amplify, as anticipated from RIT, and dominate all other waves in B_ℓ. The conjectured sequence of nonlinear interactions is tested using both frequency and wave-vector data, which are obtained by *in situ* probes and by remote sensing of the water surface with a high-speed imaging system. Our predictions of selective amplification, as well as its absence, are consistent with all of the experiments presented herein and in Part 1. Selective amplification occurs for signal-to-noise (amplitude) ratios as large as 200, and its effects are measurable within ten wavelengths of the wavemaker. When selective amplification occurs, it has a profound impact on the long-time evolution of a ripple wavetrain.

1. Introduction

Capillary–gravity waves (ripples) on a water surface exhibit a variety of instabilities (for a review, see Craik 1985). For wavetrains with moderate amplitudes, these instabilities and typical scales can be identified using the dispersion relation for an infinitesimal wavetrain:

$$c^2 := \frac{\omega^2}{k^2} = \frac{g}{k}(1+\tau)\tanh kh; \tag{1a}$$

$$\tau = \frac{Tk^2}{\rho g}. \tag{1b}$$

† Present address: Department of Naval Architecture & Marine Engineering, University of Michigan, Ann Arbor, MI 48109 USA.

‡ Former address: Institute of Geophysics & Planetary Physics, University of California, La Jolla, CA, 92093 USA.

In (1), ω is the radian frequency, g is the gravitational force per unit mass, ρ is the mass density, T is the surface tension, h is the quiescent water depth, k is the magnitude of the wavenumber vector, c is the wave celerity defined in terms of these parameters, and τ may be interpreted as the ratio of capillary and gravitational energies. These energies are equal ($\tau = 1$) for a wavetrain whose cyclic frequency is $f = \omega/2\pi = 13.6$ Hz and wavelength is $\lambda = 2\pi/k = 1.7$ cm on clean, deep water (i.e. $T = 73$ dyn/cm and $kh \gg 1$, as in our experiments and assumed hereinafter). An important instability of ripples was investigated by Wilton (1915), who found that internal resonances occur for a countable family of wavetrains corresponding to

$$\tau = \frac{1}{n}, \quad n = 2, 3, \ldots. \tag{2}$$

According to (1) and (2), Wilton ripples have the same celerity as their nth harmonic. For example, second-harmonic resonance occurs for the $n = 2$ or $\tau = \frac{1}{2}$ wavetrain, which has a frequency $f = 9.8$ Hz and wavelength $\lambda = 2.4$ cm; both the 9.8 Hz and 19.6 Hz harmonics have a celerity $c = 23.8$ cm/s. This member of Wilton ripples is also a degenerate case of a more general class of instabilities resulting from resonant three-wave interactions. Resonant triads can occur whenever the wavenumber vectors (wave vectors) $\boldsymbol{k} = (l, m)$ and frequencies ω of three wavetrains satisfy the kinematical conditions:

$$\boldsymbol{k}_1 = \boldsymbol{k}_2 \pm \boldsymbol{k}_3, \tag{3a}$$

$$\omega_1 = \omega_2 \pm \omega_3. \tag{3b}$$

(The collinear $n = 2$ Wilton ripples satisfies the sum relation of (3) with $k_1 = 2k$, $k_2 = k_3 = k$, $\omega_1 = 2\omega$, $\omega_2 = \omega_3 = \omega$.) McGoldrick (1965) first noted that ripples can satisfy (3) for a continuum of wave frequencies. Simmons (1969) used a graphical construction to show that an initial wavetrain, say $(\omega_1, \boldsymbol{k}_1)$, whose frequency exceeds 19.6 Hz ($\tau = 2$), can form two types of triads. It satisfies (3) either with two waves (summed) from a lower-frequency (closed) band, B_ℓ, or with two waves (differenced) from a higher-frequency (open-ended) band, B_h. When the initial wavetrain's frequency is less than 19.6 Hz, only the high-frequency band of allowable triads exists. Simmons also derived the dynamical interaction coefficients (see the Appendix) for a resonant triad of ripples and showed that waves in B_h could not be amplified when their amplitudes are infinitesimal relative to that of the initial wavetrain. (This result is generally true for resonant triads according to a theorem by Hasselmann 1967.) Waves in B_ℓ can be amplified; however, since the interaction coefficients vary smoothly across B_ℓ, Simmons conjectured that selective amplification of waves in B_ℓ is unlikely. Instead, all of the background waves in this frequency band are expected to amplify.

The present study is a continuation of Henderson & Hammack (1987, Part 1). In their experiments, a (test) wavetrain was generated mechanically in a channel and measured until it was extinguished by viscous damping. Results showed that wavetrains with frequencies greater than 19.6 Hz were unstable to background waves with frequencies in B_ℓ; however, in most experiments, one triad with two waves from B_ℓ was selectively amplified. The selected triad varied with the test wavetrain's frequency; however, it amplified repeatedly, regardless of the test wavetrain's amplitude, which was increased from the viscous threshold value until subharmonic cross waves evolved at the wavemaker. Part 1 did not provide an explanation for either the presence of selective amplification in some experiments, or for its absence in others.

Surprisingly, the origin of selective amplification was discovered after a new computer system was installed in the laboratory. When the previous experiments were repeated with the new system, no triads were selectively amplified. When the experiments were repeated using the older computer system, selective amplification recurred. The reason for the different results was traced to the computers' analog-output systems, which provided command signals to the wavemaker. Both devices were comparable in specification; however, the inadvertent noise level at the electrical-power frequency of 60 Hz was lower (by about $\frac{1}{5}$) for the newer device. This difference in 60 Hz noise levels, which corresponded to signal-to-noise ratios for the older computer of about 100, and about 200 for the newer computer, was sufficient to alter radically the evolution of test wavetrains. The sensitivity of ripple wavetrains to background noise, which is ubiquitous to all wave environments and generation mechanisms, is not expected from RIT (resonant interaction theory), and it has raised fundamental questions about the role of background noise. The objective of this study is to clarify that role for two types of noise: one with a spectrum that is broad-banded and the other with a spectrum containing discrete components.

An outline of the paper and our major results are as follows. Laboratory apparatus and practices are discussed in §2 with an emphasis on those aspects that differ from the detailed description in Part 1 and in Part 3 (Perlin & Hammack 1990). Experimental data are presented in §3 for test wavetrains subjected to broad-banded and discrete-component noise. No triads are selectively amplified in experiments using broad-banded noise. Instead, all of the resonant triads in B_ℓ are amplified in a manner consistent with the form of the interaction coefficient for the test wavetrain. Resonant triads with two members in B_ℓ are selectively amplified in experiments using noise with discrete component(s) in B_h. Both frequency and wave-vector spectra are measured to prove that the triads are resonant in accordance with (3). Previous results from Part 1 are reviewed to show that an inadvertent noise component at 60 Hz caused the selective amplification observed there. A conjectured explanation of selective amplification is presented, and an algorithm is described that predicts and rank orders the triad(s) that can be selectively amplified by a background wave in B_h. In brief, selective amplification is the consequence of the following nonlinear interactions, normally neglected in RIT. The test and discrete-component noise wavetrains first become directionally unstable through a degenerate quartet interaction that will be described more thoroughly in Part 3. This directional instability allows a resonant triad to form that excites a wavetrain at the difference frequency between the noise and test wavetrains. In accordance with RIT, the noise and difference wavetrains remain small; neither evolve amplitudes exceeding that of the original noise wave. Then the difference and test wavetrains, also directionally unstable, form a higher-order resonant triad that excites a new difference wavetrain. This process repeats until a resonant triad is formed among the test wavetrain and two difference wavetrains with frequencies in B_ℓ; this triad then amplifies as anticipated from RIT and dominates all others. Selective amplification occurs for signal-to-noise ratios, based on amplitude, as large as 200. All of our conclusions are summarized in §4. Numerical solutions of both the inviscid and viscous three-wave equations are presented in the Appendix.

2. Laboratory apparatus and practice

The ripple laboratory has been described in detail by Henderson & Lee (1986), Henderson & Hammack (1987, Part 1), and Perlin & Hammack (1990, Part 3). Hence, the description herein is brief and concentrates on apparatus and practices particularly relevant to the results of §3.

The wave tank was constructed of glass; it measured 91 cm wide, 183 cm long, and 15 cm deep; it was supported on the ground-floor building slab through isolation pads. The wavemaker paddle consisted of a slender right-angled aluminium wedge that was 30.4 cm wide and supported above the water surface astride the tank's long axis; the quiescent water surface intersected its midpoint. The paddle was oscillated vertically by a mini-shaker whose motion was servo-controlled with position feedback. (A ± 1 V, 25 Hz signal caused the paddle to move vertically about ± 1 mm; above 25 Hz the motion is slightly amplified and below it is slightly attenuated.) When attached to the mini-shaker, the paddle assembly had a natural vibrational frequency of 94–95 Hz. Parallel aluminium (wetted) sidewalls set adjacent to the paddle provided a test channel 91 cm long and 30.5 cm wide. A closed water-supply system provided deionized water that was filtered of organic materials and particulates with sizes above 0.2 μm. Water surface elevations at fixed locations in the tank were measured with *in situ* capacitance gauges. The diameter of the water-penetrating probe was 1.17 mm (compared to 1.47 mm in Part 1); it provided a flat response signal for frequencies up to 30 Hz (compared to 5 Hz in Part 1).

2.1. *The computer systems*

The experiments of Part 1 used a 16-bit DEC (Digital Equipment Corporation) MicroPDP-11 computer system for control and data acquisition. Sinusoidal command signals to the wave generator were provided by a Data Translation 12-bit analog-output system (DT2771) coupled with a DEC programmable clock (KWV11-C). Analog signals from wave gauges, command signals to the wavemaker, and position-feedback signals from the wavemaker paddle were digitized by a Data Translation 12-bit analog-input system (DT2782) coupled to a second programmable clock. Prior to digitizing, the analog signals were low-pass (Butterworth) filtered with a cutoff of 100 Hz, amplified 20 dB, high-pass filtered with a cutoff of 1 Hz, and amplified another 20 dB. Periodograms (energy spectra) of filtered analog signals were computed using fast Fourier transforms (FFTs); results were obtained in the frequency band 0–100 Hz with a resolution of 0.39 Hz. (These results corresponded to 2^9 data points during a 2.56 s time interval.)

The newer laboratory computer system, used in the present study, was a 32-bit DEC VAXstation II. Real-time control and data acquisition were provided by a DEC 12-bit analog-output system (AAV11-DA) and a 12-bit analog-input system (ADV11-DA); each was supported by a DEC programmable clock (KWV11-C). Software support for control, data analysis, and graphical output were provided by Signal Technology's Interactive Laboratory System. Analog signals were filtered and amplified as in Part 1. They were then digitized so that amplitude-frequency spectra (hereinafter termed frequency spectra) could be computed over the band 0–125 Hz with a resolution of 0.015 Hz. (These results correspond to 2^{14} data points in a 65.53 s time interval.)

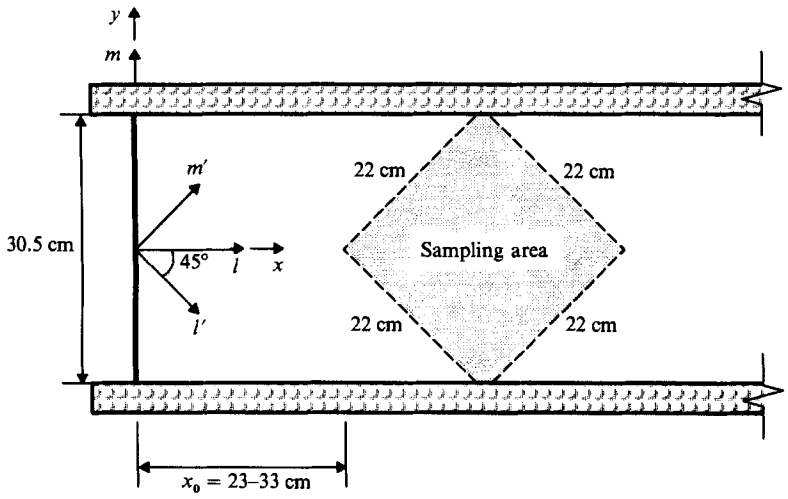

FIGURE 1. Schematic drawing (plan view) of the wave channel and coordinate system.

2.2. *The high-speed imaging system*

Semi-quantitative spatial data were obtained using a Kodak EKTAPRO 1000 Motion Analyzer. This computer-based video system records images at rates up to 1000 f.p.s. (frames per second). Each frame is composed of 240 × 192 pixels at which light intensity is measured with a resolution of 256 grey levels. Digitized frames were transferred from the EKTAPRO 1000 system to the VAXstation II computer system using a communications interface, which also allows the VAXstation II to control the imaging system.

Images of wave patterns inside the test channel were obtained using an overhead camera whose focal plane was parallel to, and 1.5 m above, the water surface. A schematic drawing (plan view) of the test channel is presented in figure 1; it shows the wavemaker, surface coordinate system, and the surface area from which quantitative spatial data were obtained. The channel was lighted by two 600 W halogen lamps in reflector housings located at the downstream end of the wave tank. The lamps were positioned above the tank, astride its centreline, and aimed at the test channel so that the incident light formed an angle of about 32° with the water surface. An opaque (white) sheet of Plexiglas was placed underneath the glass bottom of the tank in the vicinity of the test channel. A detailed description of the lighting arrangements as well as calibration tests to determine the nature of images obtained by the overhead camera are presented by Perlin & Hammack (1990, Part 3). There it is shown that video images were formed by diffuse light scattered upward by the opaque Plexiglas and refracted by the water surface so that wave crests and troughs appeared as light and dark bands, respectively, in the images. The measured light intensities, which spanned 225 grey levels, were related to water depths (or wave amplitudes). Although this relationship is not known precisely, relative grey levels among pixel sites were found to yield accurate two-dimensional amplitude–wavenumber spectra when the wave amplitudes were sufficiently small and the water surface comprised a small number of wavetrains. (Comparisons between a time series of grey levels at a single pixel site and that from a nearby wave gauge yielded a linear correlation coefficient of 0.89.) Two images viewed on the video monitor are shown in figure 2 where the test channel is inclined at an angle of 45°.

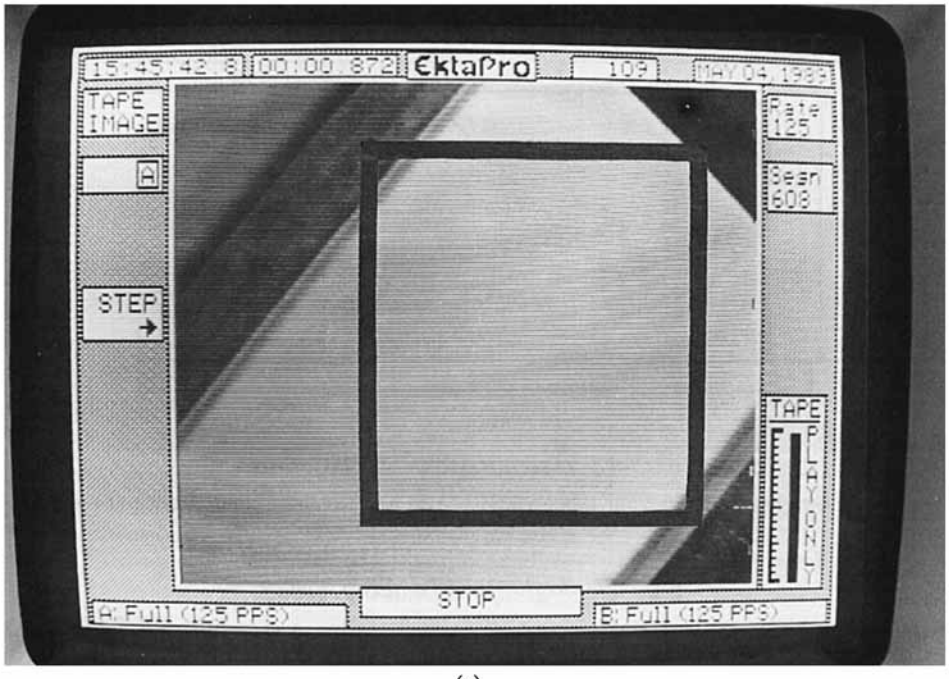

(*a*)

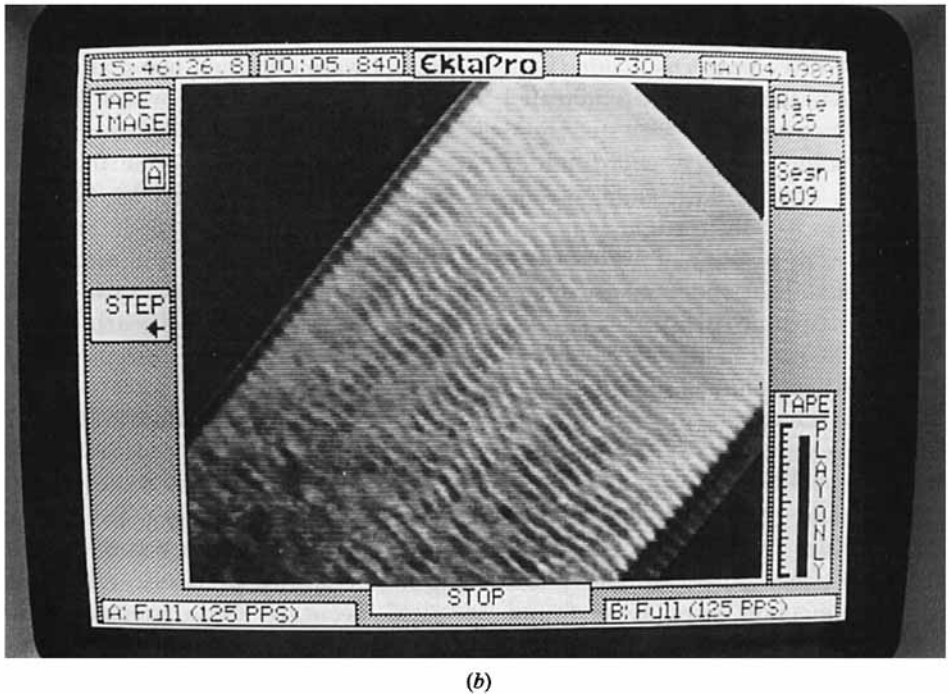

(*b*)

FIGURE 2. Overhead images of the water surface viewed on the video monitor. (*a*) Quiescent water surface; data from the square area that is delineated by a black border are used to compute the wave-vector spectrum. (*b*) 25 Hz wavetrain ($\mathscr{A}$ = 1.2 V) of experiment R25N60.01.

Images are surrounded by a frame border that provides information on the video settings, such as the 125 f.p.s. used herein. Figure 2(*a*) shows the quiescent water surface in the test channel while figure 2(*b*) shows a 25 Hz wavetrain from experiment R25N60.01. The waves are propagating from the lower left to the upper right corner of the image.

Although images contained 240×192 pixels, only 128×128 were used to compute the two-dimensional wavenumber (or wave-vector) spectrum. These 2^{14} data points fill the (22 cm × 22 cm) area delineated by the black border in figure 2(*a*) and shown schematically in figure 1. The area was oriented at an angle of 45° to the channel axis to provide accurate information for both positive and negative m-wavenumbers. (FFT computations fold information into the positive wavenumber quadrant; hence, if the image is aligned with the channel axis, waves propagating at negative angles to that channel axis would be averaged with waves at corresponding positive angles.) This image orientation limits the accuracy of calculations to waves propagating at less than $\pm 45°$ to the channel axis. The dimensions of the sampled area yield a wavenumber resolution of 0.0453 cm^{-1} or 0.284 rad/cm. The physical distance between pixel sites in the images was 0.174 cm, providing a spatial sampling rate of 5.75 cm^{-1} or 36.11 rad/cm; hence, the Nyquist (spatial) frequency is 2.87 cm^{-1} or 18.06 rad/cm. This spatial frequency corresponds to a temporal frequency of 106 Hz in the experiments; temporal data show very little energy at this frequency.

Images were obtained for analysis in the following manner. First, an experiment was performed with an *in situ* wave gauge. Then, the gauge was removed to provide an uninterrupted overhead view. The quiescent water surface was imaged, and the experiment was repeated and recorded on video tape at 125 f.p.s. The background grey level for the quiescent water surface at each pixel site was subtracted from each image; then the mean grey level for the array was subtracted. The resulting two-dimensional array of grey levels, which provided a measure of the vertical deformation of the water surface from its quiescent position, was then used to calculate the wave-vector spectrum.

3. Evolution of ripple wavetrains in the presence of background noise

Here, experimental results are presented for the evolution of ripple wavetrains in the presence of smaller background waves. Both the test and background wavetrains are generated simultaneously by the wavemaker. This procedure raises the following cautionary note. The dynamics of all wavemakers and the coupling between the wavemaker and water (e.g. see Flick & Guza 1980) are inherently nonlinear. (Even the electro-dynamics of the analog-output devices that provide command signals to the wavemaker are weakly nonlinear.) Hence, when the wavemaker is commanded to oscillate at a single frequency, additional motions at superharmonic frequencies occur. When commanded to oscillate at two frequencies, additional motions at superharmonic, sum, and difference frequencies occur. All of these motions, as well as the nonlinear coupling with the water, generate free water waves that satisfy (1) and coexist with bound waves of the same frequencies that do not satisfy (1). These waves are small when the dynamics are weakly nonlinear, as they are herein. Unfortunately, capillary–gravity waves can be affected profoundly by small background waves. Accordingly, we measured both the command signal to, and the feedback signals from, the wavemaker in all experiments; these data are presented when appropriate.

Experiment	Test-wave frequency f_1 (Hz)	Background-wave frequency f_0 (Hz)	B_ℓ (Hz)	$B_{h_{min}}$ (Hz)	Resonant triad frequencies (Hz)					
					Measured			Theoretical		
					f_1	f_2	f_3	f_1	f_2	f_3
CG2212†	21.88	60.16	5.80–16.20	27.80	21.88	5.86	16.02	—	—	—
CG2512†	25.00	60.16	4.94–20.06	29.94	25.00	10.16	14.84	25.00	10.16	14.84
CG2797†	26.95	60.16	4.52–22.48	31.52	26.95	6.25	20.70	26.95	6.26	20.69
								26.95	14.43	12.52
CG3082†	30.08	60.16	3.98–26.02	33.98	30.00	—	—	—	—	—
CG3278†	32.03	60.16	3.63–28.37	35.63	32.03	—	—	—	—	—
CG3480†	33.98	60.16	1.10–32.90	35.10	33.98	26.17	7.81	33.98	26.18	7.80
								33.98	15.6	18.38
CG3609†	35.94	60.16	1.10–34.90	37.10	35.94	24.22	11.72	35.94	24.22	11.72
CG3865†	37.89	60.16	1.10–36.90	39.10	37.89	22.27	15.63	37.89	22.27	15.62
								37.89	6.65	31.24
								37.89	24.59	13.30
								37.89	11.29	26.60
								37.89	15.31	22.58
								•	•	•
CG4055†	39.84	60.16	0.91–39.09	40.91	44.25	19.92	19.92	39.84	20.32	19.52
CG4450†	43.75	60.16	0.91–43.09	44.91	43.75	16.41	27.34	43.75	16.41	27.34
								43.75	10.93	32.82
								43.75	21.89	21.86

CG4645†	45.70	60.16	0.91–45.09	46.91	45.70	14.45	31.64	45.70	14.46	31.24
								45.70	16.78	28.92
								45.70	12.14	33.56
								45.70	21.42	24.28
								45.70	2.86	42.84
								●	●	●
R25N57.01	25.00	57.00	4.94–20.06	29.94	25.00	7.00	18.00	25.00	7.00	18.00
								25.00	11.00	14.00
R25N57.10	25.00	57.00	4.94–20.06	29.94	25.00	7.00	18.00	25.00	7.00	18.00
					25.00	11.00	14.00	25.00	11.00	14.00
R25N52.05	25.00	52.00	4.94–20.06	29.94	—	—	—	—	—	—
R25N59.01	25.00	59.50	4.94–20.06	29.94	25.00	9.50	15.50	25.00	9.50	15.50
								25.00	6.00	19.00
								25.00	13.00	12.00
		60.00			25.00	10.00	15.00	25.00	10.00	15.00
								25.00	5.00	20.00
		60.50			25.00	10.50	14.50	25.00	10.50	14.50
R25N60.01	25.00	60.00	4.94–20.06	29.94	25.00	10.00	15.00	25.00	10.00	15.00
								25.00	5.00	20.00

† Experiment from Henderson & Hammack (1987, Part 1) where the frequency resolution was 0.39 Hz and the 60.16 Hz background wave was added inadvertently.

TABLE 1. Summary of experiments on ripple wavetrains in the presence of noise spectra with discrete components. Theoretical values are based on the (inviscid) algorithm of figure 5. $h = 5$ cm, $T = 73$ dyn/cm. ● indicates that more resonant triads are available.

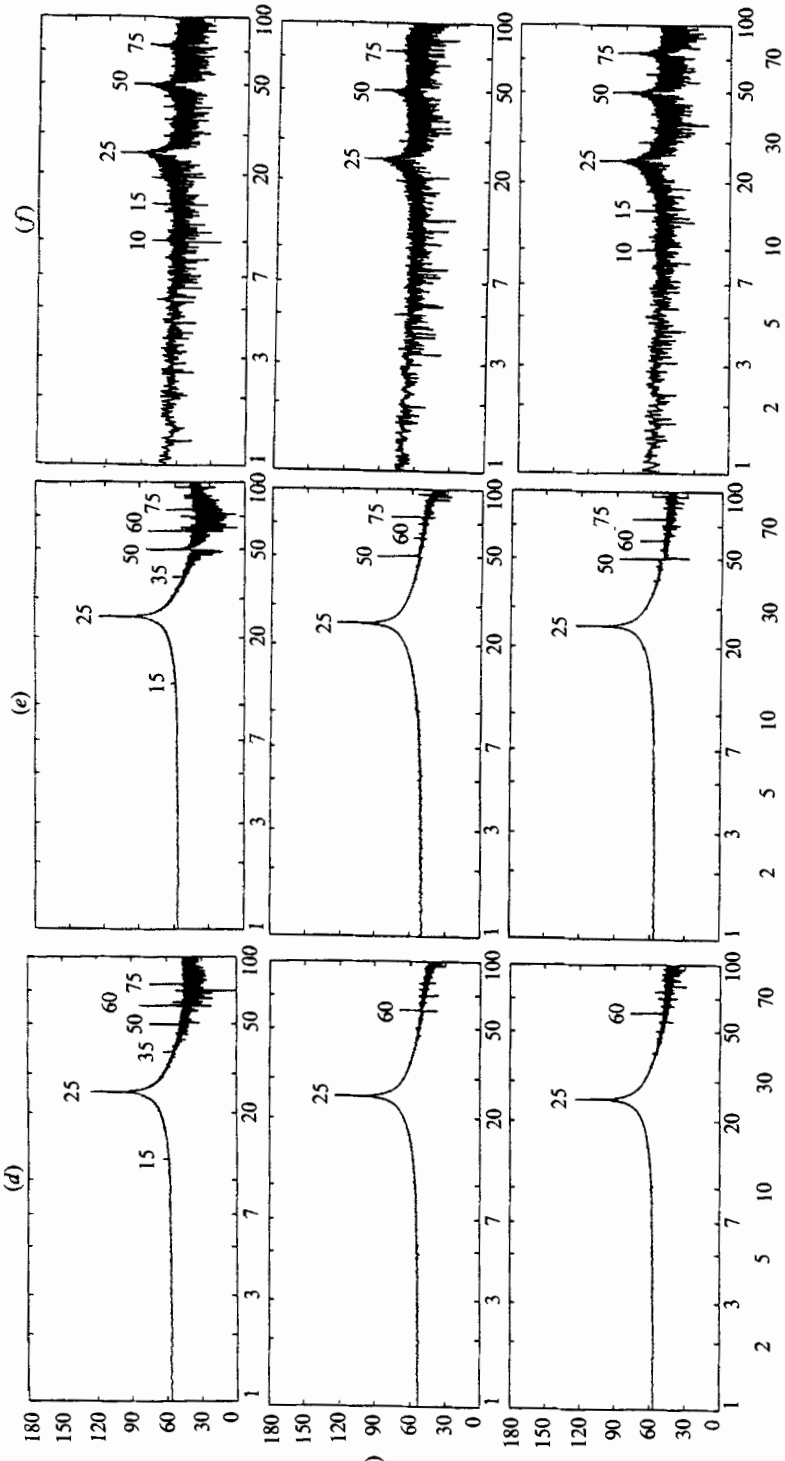

FIGURE 3. Amplitude–frequency spectra for a 25 Hz test wavetrain ($\mathscr{A} = 1.2$ V); $h = 5$ cm, $T = 73$ dyn/cm. Row (*a*) MicroPDP-11 computer command to wavemaker; row (*b*) VAXstation II computer command to wavemaker; row (*c*) VAXstation II computer command to wavemaker with 60 Hz signal ($\mathscr{A} = 0.0048$ V) added; column (*d*) command signals; column (*e*) feedback signals; column (*f*) wave-gauge signal at $(x, y) = (7, -4.7)$ cm.

3.1. *Discrete-component spectral noise*

Previous results from Part 1 are summarized in table 1 for eleven experiments labelled CG*xxxx*. The measured frequencies (resolved to 0.39 Hz) are given for the test wavetrain and wavetrains selectively amplified from background waves. Two waves from B_ℓ were selectively amplified in nine experiments; no selective amplification occurred in two experiments. The frequency range of B_ℓ and the lower frequency limit of B_h for each test wavetrain are also presented in table 1. These ranges were calculated by first noting that wavetrains at the frequency limits arise from considerations of collinear triads (see Part 1). Hence, the vector (sum) relation of (3*a*) can be replaced by a scalar relation on wave-vector magnitudes. Second, we allow a finite amount of detuning $\mathscr{D}$ defined by

$$\mathscr{D} := \frac{k_2 + k_3}{k_1}, \tag{4}$$

so that $\mathscr{D} = 1$ corresponds to perfect resonance; $\mathscr{D} < 1$ implies detuning, since (3*a*) would not be satisfied even for collinear wave vectors; and $\mathscr{D} > 1$ implies perfect resonance for a noncollinear triad. In the calculations of table 1 we have taken $\mathscr{D} = 0.98$ to allow for the small detuning that is consistent with experimental observations. (These frequency ranges differ from those quoted in Part 1, since less detuning was allowed there.)

As mentioned previously, selective amplification in the experiments of Part 1 was a consequence of 60 Hz electrical noise from the analog-output device that provided command signals to the wavemaker. The analog-output device in the newer computer system also produced 60 Hz noise; however, its level was lower and no selective amplification occurred. These results are illustrated in figure 3, which shows frequency spectra for the command signals (column *d*), wavemaker feedback signals (column *e*), and wave gauge signals (column *f*) in three experiments (rows *a*, *b*, *c*). Each experiment used a 25 Hz test wavetrain whose command-signal amplitude was $\mathscr{A}_{25} = 1.2$ V. (The wave gauge was located at $(x, y) = (7, -4.7)$ cm.) The spectra in row (*a*) were obtained using the older computer system (MicroPDP-11) to provide the command signal; these results correspond to experiment CG2512 in table 1 (figure 10 in Part 1). The spectra in row (*b*) were obtained using the newer computer system (VAXstation II) to provide the command signal. The spectra in row (*c*) were obtained by adding a 60 Hz signal, with $\mathscr{A}_{60} = 0.0048$ V, to the 25 Hz signal of the VAXstation II. (In fact, 0.0048 V is the smallest voltage resolved by the analog-output device; hence, the superposed 60 Hz signal is rectangular, rather than sinusoidal.) The spectral amplitudes are presented in arbitrarily scaled units of dB (20 dB corresponds to a factor of 10; in general, log (factor) = (dB/20)). The same dB scale is used for the spectra in each column of figure 3 so that relative comparisons are meaningful.

The wave-gauge frequency spectra in column (*f*) of figure 3 show the following: selective amplification of 10 and 15 Hz wavetrains in the experiment of row (*a*), as found in Part 1; no selective amplification in the experiment of row (*b*); selective amplification of 10 and 15 Hz wavetrains in the experiment of row (*c*). Hence, the addition of a small 60 Hz signal (which decreased the signal-to-noise ratio by about 3.7) in the command signal of the newer computer system precipitates selective amplification. In Part 1 it was conjectured that the 10 and 15 Hz wavetrains were resonant with the 25 Hz wavetrain because of their relatively large amplitudes and the cycling of their energies during propagation. The water-surface imaging system

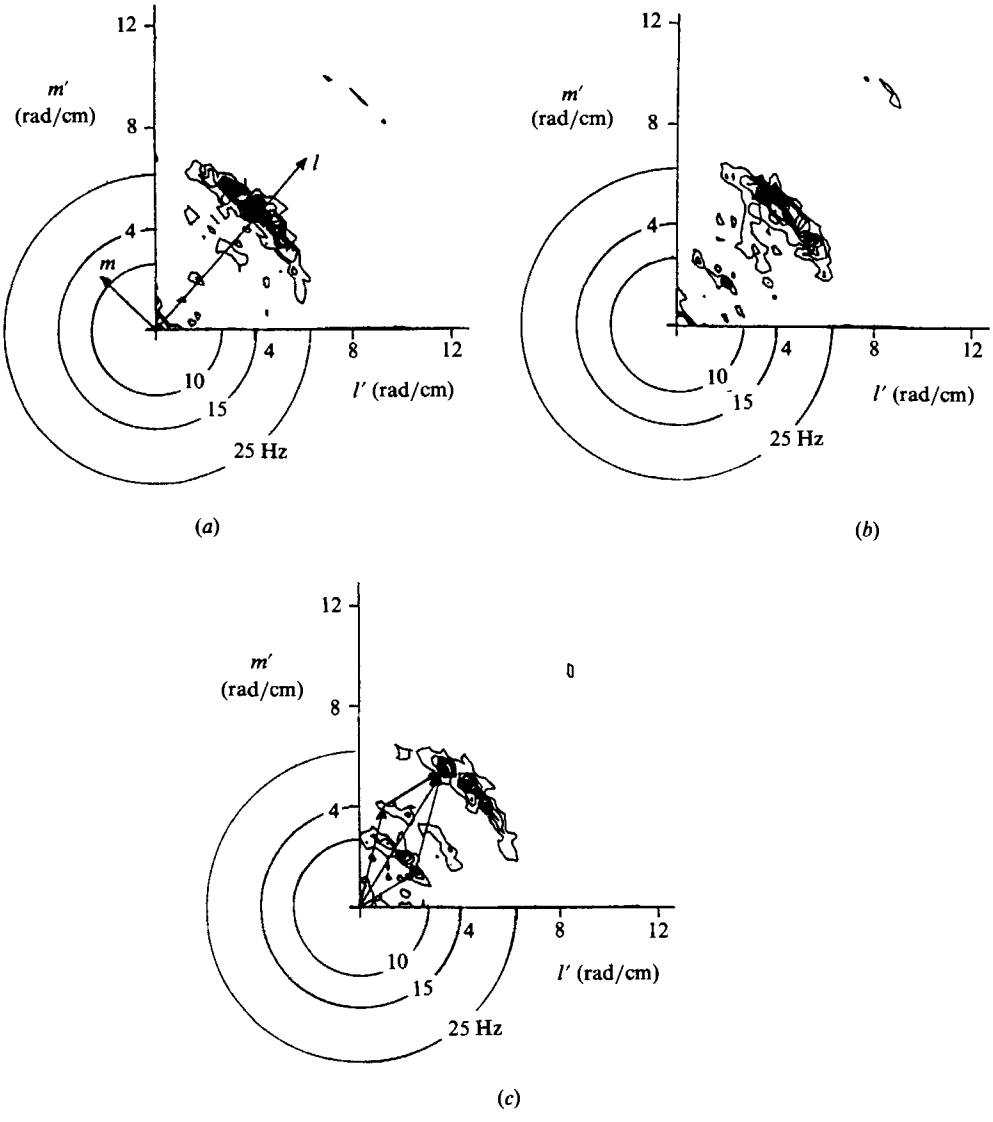

FIGURE 4. Contour maps of wave-vector spectra for experiments using a 25 Hz test wavetrain; $h = 5$ cm, $T = 73$ dyn/cm. (*a*) $\mathscr{A}_{25} = 1.2$ V, $\mathscr{A}_{60} = 0.0048$ V, $x_0 = 33$ cm; (*b*) $\mathscr{A}_{25} = 1.2$ V, $\mathscr{A}_{60} = 0.010$ V, $x_0 = 33$ cm; (*c*) $\mathscr{A}_{25} = 0.6$ V, $\mathscr{A}_{60} = 0.060$ V, $x_0 = 23$ cm.

allows us to test this conjecture by providing wave-vector spectra that determine whether the resonance condition of (3*a*) is satisfied. Contour maps of wave-vector spectra for three experiments are presented in figure 4. The results in figure 4(*a*) correspond to the experiment of row (*c*) in figure 3; the results in figure 4(*b*) correspond to an experiment in which the 60 Hz signal of the VAXstation II is increased to equal that of the MicroPDP-11; the results of figure 4(*c*) correspond to an experiment in which the amplitude of the 25 Hz wavetrain is reduced ($\mathscr{A}_{25} = 0.6$ V) and the amplitude of the 60 Hz signal is increased ($\mathscr{A}_{60} = 0.06$ V). All of the experiments in figure 4 show that the 25 Hz wavetrain has directionally spread its energy along a (nearly) circular arc corresponding to its dispersion curve (circle). This

phenomenon is in consequence of a Benjamin–Feir-type instability to transverse modulations, i.e. a degenerate resonant quartet interaction, which is described in Part 3. Dispersion circles for 10 and 15 Hz wavetrains are also shown in figure 4. The dominant spectral amplitudes in all three experiments lie along the dispersion circles for the 10, 15 and 25 Hz wavetrains (to within the computational resolution of 0.284 rad/cm). The directional spreading of energy for each of these wavetrains enables them to satisfy easily the wave-vector equation of (3*a*); hence, these wavetrains form resonant triads as conjectured in Part 1. Sample wave-vector diagrams of (3*a*) are shown in figure 4(*c*). Note that they can be rotated to many orientations, and that the 10 and 15 Hz vectors can be interchanged; hence, there is a spatial distribution of (10, 15, 25) Hz triads in the channel.

The results in column (*f*) of figure 3 suggest that selective amplification is caused by an exceedingly low level of 60 Hz noise in the command signal. The spectral amplitudes of the command signals in column (*d*) of figure 3 are similar for frequencies less than 30 Hz showing a dominant peak with an amplitude of 124 dB at 25 Hz. (Since this amplitude is known to be 1.2 V, voltages can be found at other frequencies.) Above 30 Hz, the command signal of the MicroPDP-11 contains a discrete component at 60 Hz with a peak of 0.0109 V. (Other peaks correspond to superharmonic frequencies at 50 and 75 Hz, both 0.0036 V, and sum and difference frequencies at 70, 65, 35, and 15 Hz, all less than 0.001 V.) The command spectrum of the VAXstation II (row *b*, column *d*) contains only a 60 Hz peak with an amplitude of 0.0019 V, which is about $\frac{1}{5}$ that of the MicroPDP-11. Even when a 60 Hz signal with an amplitude of 0.0048 V is intentionally added to the command signal of the VAXstation II, no additional discrete components occur in its spectrum. Hence, the newer analog-output device is also less nonlinear than the older system. Selective amplification occurs when the amplitude of the 60 Hz noise in the command signals exceeds 0.0019 V + 0.0048 V $\approx$ 0.0070 V, which is about $\frac{1}{200}$ or 46 dB below that of the 25 Hz signal. This measured threshold is lower than that predicted by a viscous RIT (see the Appendix, §A.2), which requires the noise component to have a threshold amplitude about $\frac{1}{70}$ that of the test wavetrain.

3.1.1. *Explanation of selective amplification*

We conjecture that selective amplification of two wavetrains in B_ℓ, by a test wavetrain f_1 of moderate amplitude and a small-amplitude background wavetrain f_0 in B_h, occurs as follows. First, the test and background wavetrains become directionally unstable as seen in figure 4. This step is crucial to selective amplification because the test and noise wavetrains are initially collinear and generally cannot satisfy (3*a*). The directional instability allows the wavetrains with the correct frequencies (3*b*) to also have the correct angles to satisfy (3*a*). Hence, they form a resonant triad with the difference wavetrain ($f_0 - f_1$). The difference wavetrain cannot amplify, in accordance with Hasselmann's theorem; however, numerical computations (see the Appendix) show that it does exchange energy with f_0. The difference wavetrain then becomes directionally unstable so that a new resonant triad with frequencies ($f_1, f_0 - f_1, 2f_1 - f_0$) forms. Again, the new difference wavetrain cannot amplify, but exchanges energy with the previous difference wavetrain (see the Appendix). This process continues until a difference wavetrain with a frequency, say f_2, in B_ℓ is excited and becomes directionally unstable. Then a resonant triad forms with frequencies ($f_1, f_2, f_3 = f_1 - f_2$). Since the small background waves in this resonant triad have frequencies in B_ℓ, they can exchange energy with the test wavetrain and amplify (see the Appendix).

The above scenario comprises exceedingly weak nonlinear interactions that are normally ignored; yet, when they occur, they determine the wavetrains that will dominate an experiment. For definiteness, consider a test wavetrain with a steepness ak that is $O(\alpha)$ and a discrete-component noise wavetrain whose steepness is $O(\beta)$ such that $\beta \ll \alpha \ll 1$. Then the minimum interaction order needed to selectively amplify a resonant triad with two waves in B_ℓ is $O(\alpha^2\beta)$, and directional instabilities of $O(\alpha^3)$ are required to satisfy (3*a*). In fact, additional difference waves, each smaller in wave steepness, were required in all of the experiments reported herein and most of those in Part 1 before the triad with waves in B_ℓ was selectively amplified. For example, the 25 Hz wavetrain used in the experiments of figures 3 and 4, and throughout the study presented herein, was shown in Part 1 to have $\alpha_{25} \approx 0.2$. Since a 60 Hz command signal of about $\frac{1}{200}$ that of the 25 Hz wave caused selective amplification, and since the wavenumber of a 60 Hz wavetrain is about twice that of the 25 Hz wavetrain, we estimate $\beta_{60} \approx 0.002$. The first resonant triad interaction produces a 35 Hz wavetrain whose steepness is $O(\alpha\beta) \approx 4 \times 10^{-4}$; the second resonant triad interaction produces a 10 Hz wavetrain whose steepness is $O(\alpha^2\beta) \approx 8 \times 10^{-5}$; the third resonant triad interaction produces a 15 Hz wavetrain whose steepness is $O(\alpha^3\beta) \approx 1.6 \times 10^{-5}$ (hereinafter, we refer to each succeeding resonant triad as *higher-order*). Even though these higher-order triad interactions are exceedingly weak, their impact is measurable within ten wavelengths of the wavemaker. Experiments also indicate that if the low-frequency wavetrains in the selected triad have a difference wavetrain in B_ℓ, then the selected triad can cause the amplification of an additional resonant triad, which comprises wavetrains with even smaller steepnesses. (This triad, in turn, may produce another higher-order triad.) The above scenario is contained in an algorithm that is shown schematically in figure 5; results of applying the algorithm to the experiments of Part 1 are given in table 1. Note that the algorithm correctly predicts both the selectively amplified wavetrains in those experiments and the absence of selective amplification for two experiments. The algorithm also predicts the higher-order resonant triads, which can be selectively amplified for some test and noise wavetrains; these triads are ranked according to their expected order of occurrence.

3.1.2. *Further experiments on selective amplification*

Further tests of the conjectured explanation of selective amplification given above are presented in this section. First, noise spectra with discrete components at frequencies other than 60 Hz are introduced and their spectral amplitudes, relative to the amplitudes of the test wavetrains, are varied. Then the effects of varying the spectral amplitude of the noise component relative to the surrounding spectral levels are examined.

Figure 6 shows the frequency and wave-vector spectra obtained during an experiment (R25N57.01) that used a 25 Hz test wavetrain and a 57 Hz noise wavetrain whose command signal amplitudes were 1.2 V and 0.001 V, respectively. For these waves, the algorithm of figure 5 (see table 1) predicts the possibility of selectively amplifying two resonant triads with frequencies of (25, 7, 18) Hz and (25, 11, 14) Hz through nonlinear interactions of $O(\alpha^3\beta)$ and $O(\alpha^6\beta^2)$, respectively. The frequency spectrum of figure 6(*a*), which was obtained from wave-gauge data at $(x, y) = (7, -4.7)$ cm, clearly shows spectral peaks at 7 and 18 Hz. The wave-vector spectrum in figure 6(*b*) confirms that the 7 and 18 Hz wavetrains are resonant with the 25 Hz wavetrain. Dispersion curves for each of these wavetrains and a sample wave-vector diagram of (3*a*) are superposed on the wave-vector spectrum. Note that

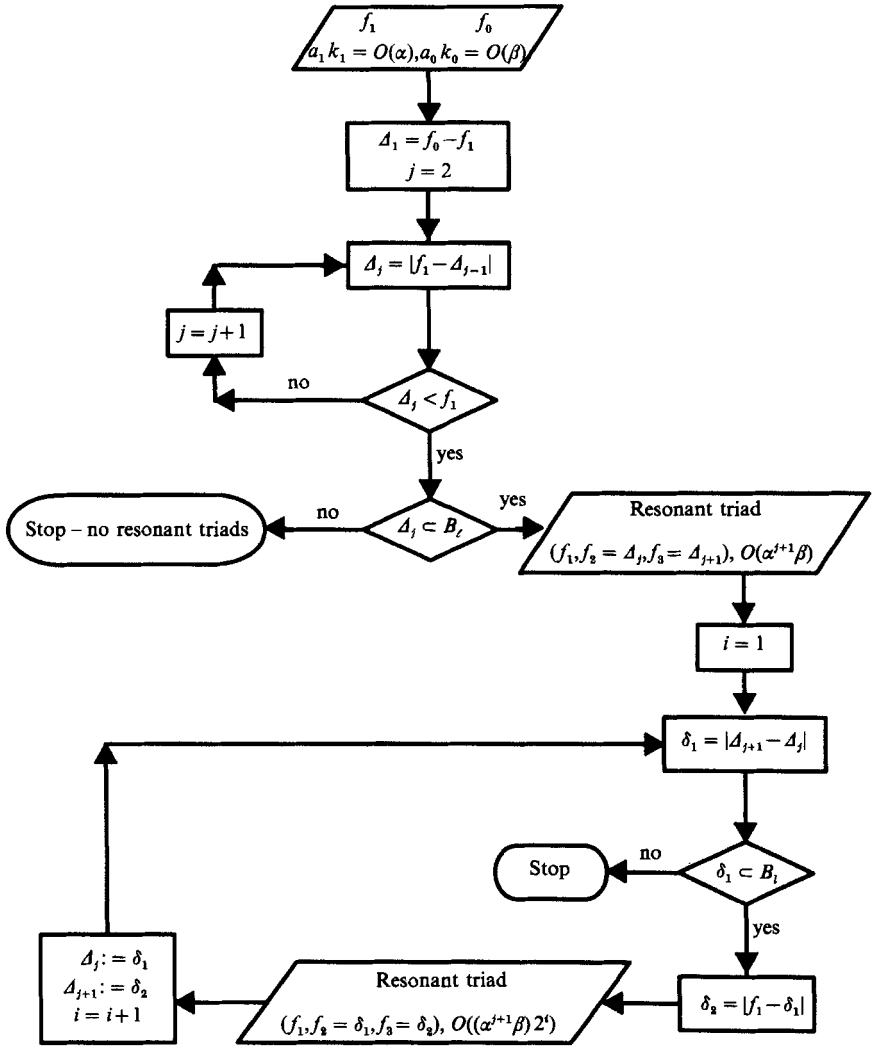

FIGURE 5. Algorithm for calculating the resonant triads selectively amplified from the low-frequency band B_ℓ of a test wavetrain f_1 when a discrete infinitesimal background wave f_0 in the high-frequency band B_h is present. The steepnesses of test and background wavetrains are $O(\alpha)$ and $O(\beta)$, respectively, with $\beta \ll \alpha \ll 1$.

each of the spectral peaks for these three wavetrains can be connected by a wave-vector diagram such as the one shown, i.e. dominant orientations exist in the spatial distribution of this resonant triad.

It is not surprising that the higher-order (25, 11, 14) Hz resonant triad was not selectively amplified in the experiment shown in figure 6, since the small-amplitude 60 Hz noise in the experiments of Part 1 never selectively amplified higher-order triads (see §3.1.1). In order to determine if higher-order triads can be amplified, the command signal amplitude of the 57 Hz noise wavetrain was increased to $\mathscr{A}_{57}$ = 0.1 V. Frequency spectra for this experiment (R25N57.10) at seven downstream positions are shown in figure 7. Spectral peaks proliferate at the first measurement station (x = 7 cm), occurring at a variety of sum and difference frequencies among the 25 Hz wavetrain, its superharmonic, and the 57 Hz wavetrain. The spectral

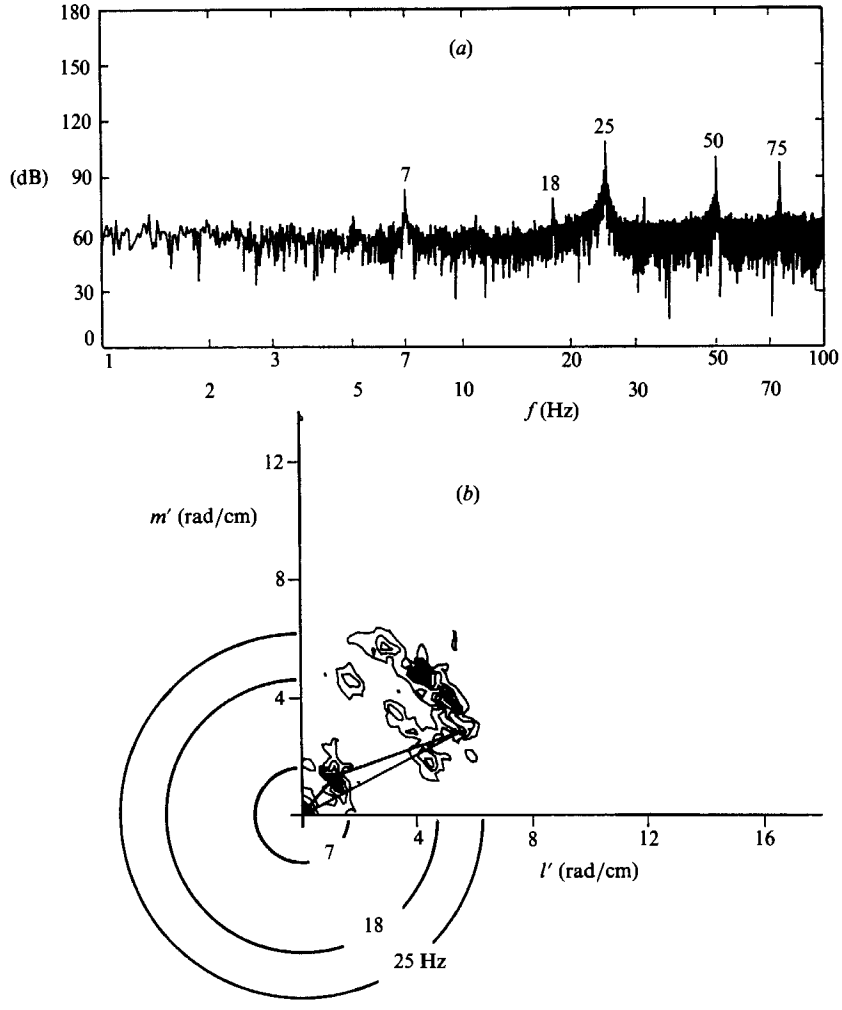

FIGURE 6. Wave amplitude spectra for a 25 Hz test wavetrain ($\mathscr{A} = 1.2$ V) in the presence of a 57 Hz background wavetrain ($\mathscr{A} = 0.01$ V); $h = 5$ cm, $T = 73$ dyn/cm. (*a*) Frequency spectrum at $(x, y) = (7, -4.7)$ cm; (*b*) contour map of wave-vector spectrum, $x_0 = 33$ cm.

amplitudes at 7 and 18 Hz are already nearly as large as that at 25 Hz; the 57 Hz peak is quite small, less than that at 60 Hz. During evolution the peaks at 11 and 14 Hz disappear and re-emerge, indicating a resonant cycling of energy. In addition, all of the spectral peaks, except those at 7, 11, 14, 18, and 25 Hz, disappear with the 7 Hz wavetrain dominant at the last station. The wave-vector spectrum, obtained from a sampling region beginning at $x_0 = 33$ cm, is shown in figure 8 with dispersion curves superposed at the frequencies of 7, 11, 14, 18 and 25 Hz. The 7 Hz wavetrain is again dominant; in fact, very little energy remains in the 25 Hz wavetrain. It is also apparent from figure 8 that the 11 and 14 Hz wavetrains form a resonant triad with the test wavetrain. Hence, selective amplification of higher-order triads does occur when the amplitude of the component-noise wavetrain, relative to that of the test wavetrain, is increased.

Figure 9 shows the frequency and wave-vector spectra obtained in an experiment (R25N52.05) that used a 25 Hz test wavetrain and a 52 Hz noise wavetrain; the

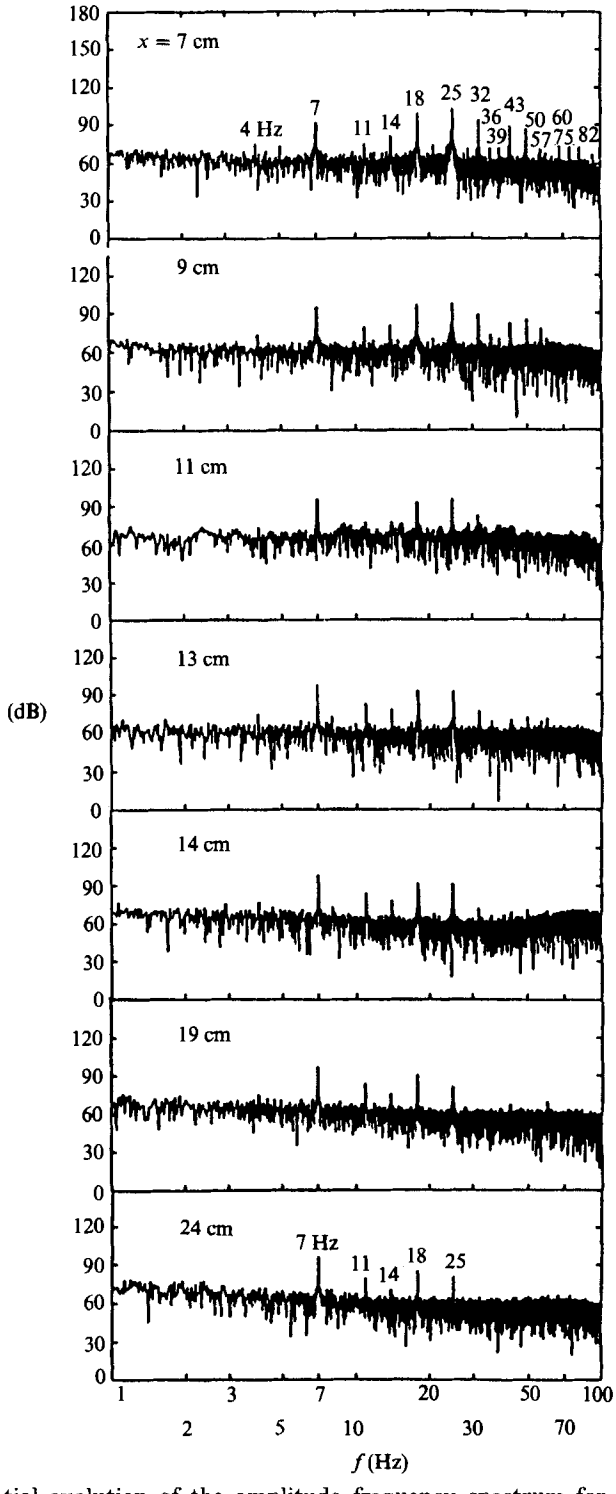

FIGURE 7. Spatial evolution of the amplitude–frequency spectrum for a 25 Hz test wavetrain ($\mathscr{A} = 1.2$ V) in the presence of a 57 Hz background wavetrain ($\mathscr{A} = 0.10$ V); $h = 5$ cm, $T = 73$ dyn/cm.

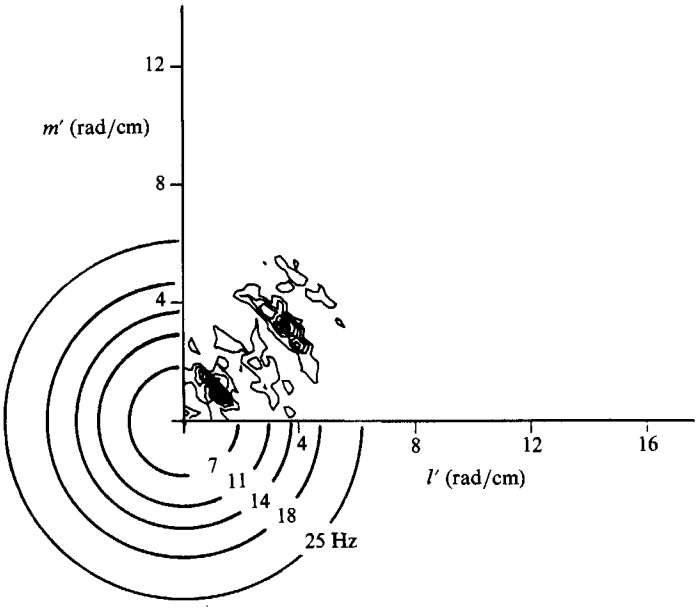

FIGURE 8. Contour map of amplitude–wave-vector spectrum for a 25 Hz test wavetrain ($\mathscr{A} = 1.2$ V) in the presence of a 57 Hz background wavetrain ($\mathscr{A} = 0.10$ V); $h = 5$ cm, $T = 73$ dyn/cm, $x_0 = 33$ cm.

command signal amplitudes were 1.2 V and 0.05 V, respectively. The algorithm of figure 5 predicts that no resonant triads should be selectively amplified from B_ℓ in this experiment. According to that algorithm, the 25 and 52 Hz wavetrains should directionally spread their energy and excite a resonant triad with a 27 Hz difference wavetrain, whose amplitude should not exceed that of the 52 Hz wavetrain. These waves appear in the frequency spectrum of figure 9(*a*); only the 25 Hz and 27 Hz wavetrains appear in the wave-vector spectrum of figure 9(*b*), since the amplitude of the 52 Hz wavetrain is below that of the first contour level. Next, the 27 and 25 Hz wavetrains interact to yield a difference wavetrain of 2 Hz, and an amplitude peak at 2 Hz appears in the frequency spectrum of figure 9(*a*). However, the wave vectors for these three waves cannot satisfy (3*a*) so that the 2 Hz difference wavetrain must be bound, and it must have a wavenumber of about 0.39 rad/cm, which differs from the free-wave value of 0.16 rad/cm. The wave-vector spectrum of figure 9(*b*) shows an extremum at $k = 0.4$ rad/cm, in agreement with expectations. No extremum is apparent at $k = 0.16$ rad/cm; however, our spatial resolution of wavenumbers (0.284 rad/cm) prevents definitive conclusions. It should also be noted that the initially collinear 25 and 52 Hz wavetrains interact to form a 27 Hz bound wave, whose (bound) wavenumber magnitude is 4.63 rad/cm. A circle with a radius of 4.63 rad/cm is shown in figure 9(*b*), and the spectrum shows significant amplitudes for these 27 Hz bound waves, as in figure 9(*a*).

There is another aspect of wavetrain evolution in the experiment of figure 9 that should be emphasized. A 25 Hz (free) wavetrain and a collinear 2 Hz (bound) wavetrain interact to form a collinear 23 Hz wavetrain, whose wavenumber magnitude is 5.94 rad/cm, which happens to satisfy the dispersion relation. Hence, the 23 and 25 Hz wavetrains are resonant and form a degenerate resonant quartet that corresponds to the classical longitudinal Benjamin–Feir instability. (See Part 3

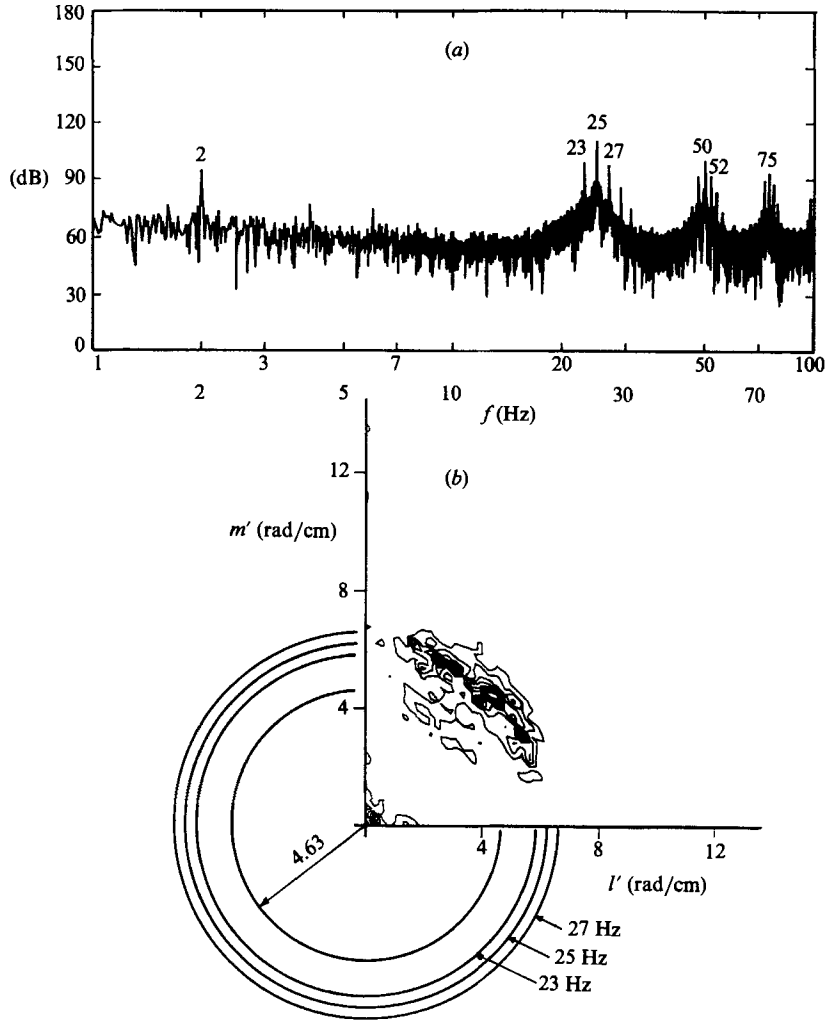

FIGURE 9. Wave amplitude spectra for a 25 Hz test wavetrain ($\mathscr{A}$ = 1.2 V) in the presence of a 52 Hz background wavetrain ($\mathscr{A}$ = 0.05 V); h = 5 cm, T = 73 dyn/cm. (*a*) Frequency spectrum at (x, y) = (7, −4.7) cm; (*b*) contour map of wave-vector spectrum, x_0 = 33 cm.

for a more detailed description of Benjamin–Feir type instabilities for ripples.) According to analytical predictions for the Benjamin–Feir instability (see Part 3), the most unstable sidebands for a 25 Hz wavetrain, whose steepness is 0.2, have frequencies of 21.9 and 28.3 Hz; the unstable frequency band is 20.7–29.7 Hz. All of these predictions are consistent with the frequency and wave-vector spectra of figure 9. Unlike frequency spectra in previous experiments that use the 25 Hz test wavetrain, figure 9(*a*) shows substantial sideband amplitudes, and the wave-vector spectrum shows significant amplitudes along the dispersion curve of a 23 Hz wavetrain. (Difference wavetrains in the previous experiments were outside the unstable band for Benjamin–Feir instabilities.) Hence, the selection mechanism for resonant triads can also selectively amplify resonant quartet interactions, at least when resonant triads are not possible.

Figure 10 shows results from an experiment that used a 25 Hz test wavetrain

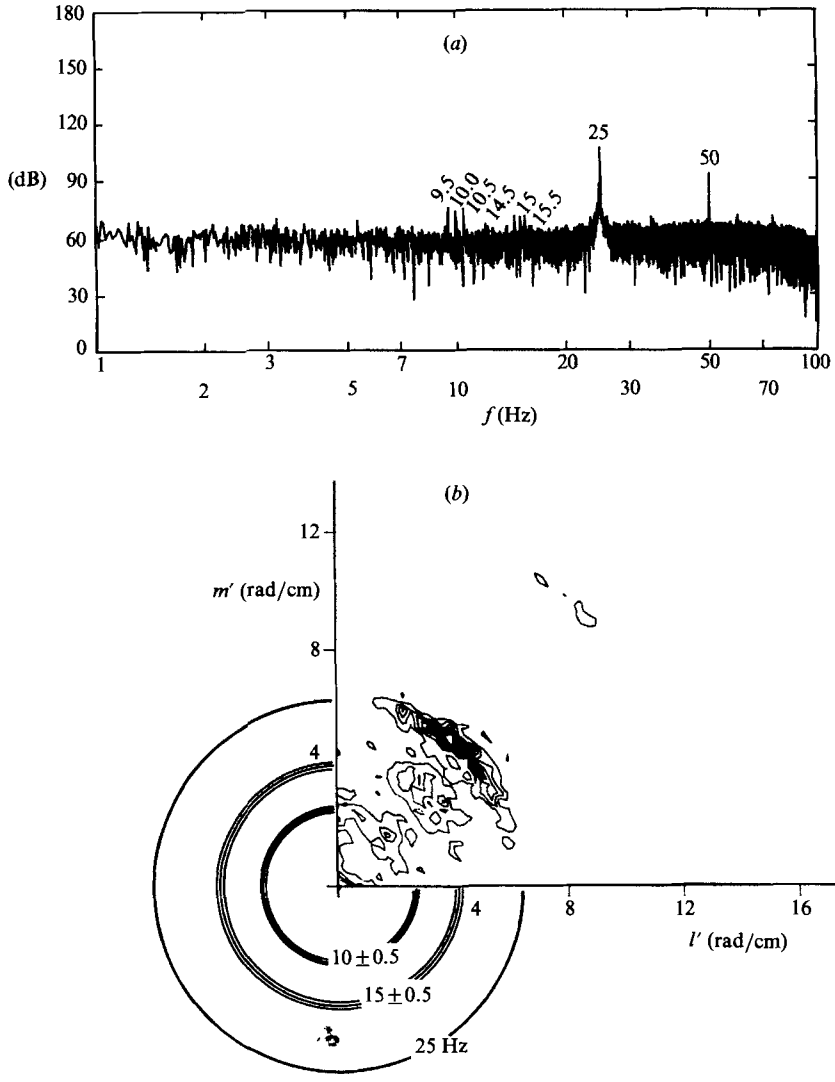

FIGURE 10. Wave amplitude spectra for a 25 Hz test wavetrain ($\mathscr{A} = 1.2$ V) in the presence of three background wavetrains with frequencies 59.5, 60, and 60.5 Hz ($\mathscr{A} = 0.01$ V for each of the background waves); $h = 5$ cm, $T = 73$ dyn/cm. (*a*) Frequency spectrum at $(x, y) = (7, -4.7)$ cm; (*b*) contour map of wave-vector spectrum, $x_0 = 33$ cm.

($\mathscr{A}_{25} = 1.2$ V) and a noise spectrum that contained three discrete components in B_h. The noise components had frequencies of 59.5, 60, and 60.5 Hz and command signal amplitudes of 0.01 V. In this experiment, selective amplification by each noise component appears to occur simultaneously. The frequency spectrum of figure 10(*a*) shows the selective amplification of three wave pairs (9.5/15.5 Hz, 10/15 Hz, 10.5/14.5 Hz), as predicted by the algorithm of figure 5. The wave-vector spectrum in figure 10(*b*) shows bands about the dispersion curves for these waves. Note that the contour lines in this spectrum are scaled identically to those in the experiment of figure 4(*b*), which used only a 60 Hz noise wavetrain. Comparing these two wave-vector spectra confirms the increase in wave energy near the 10 and 15 Hz dispersion curves, as expected from the amplification of nearby resonant wavetrains.

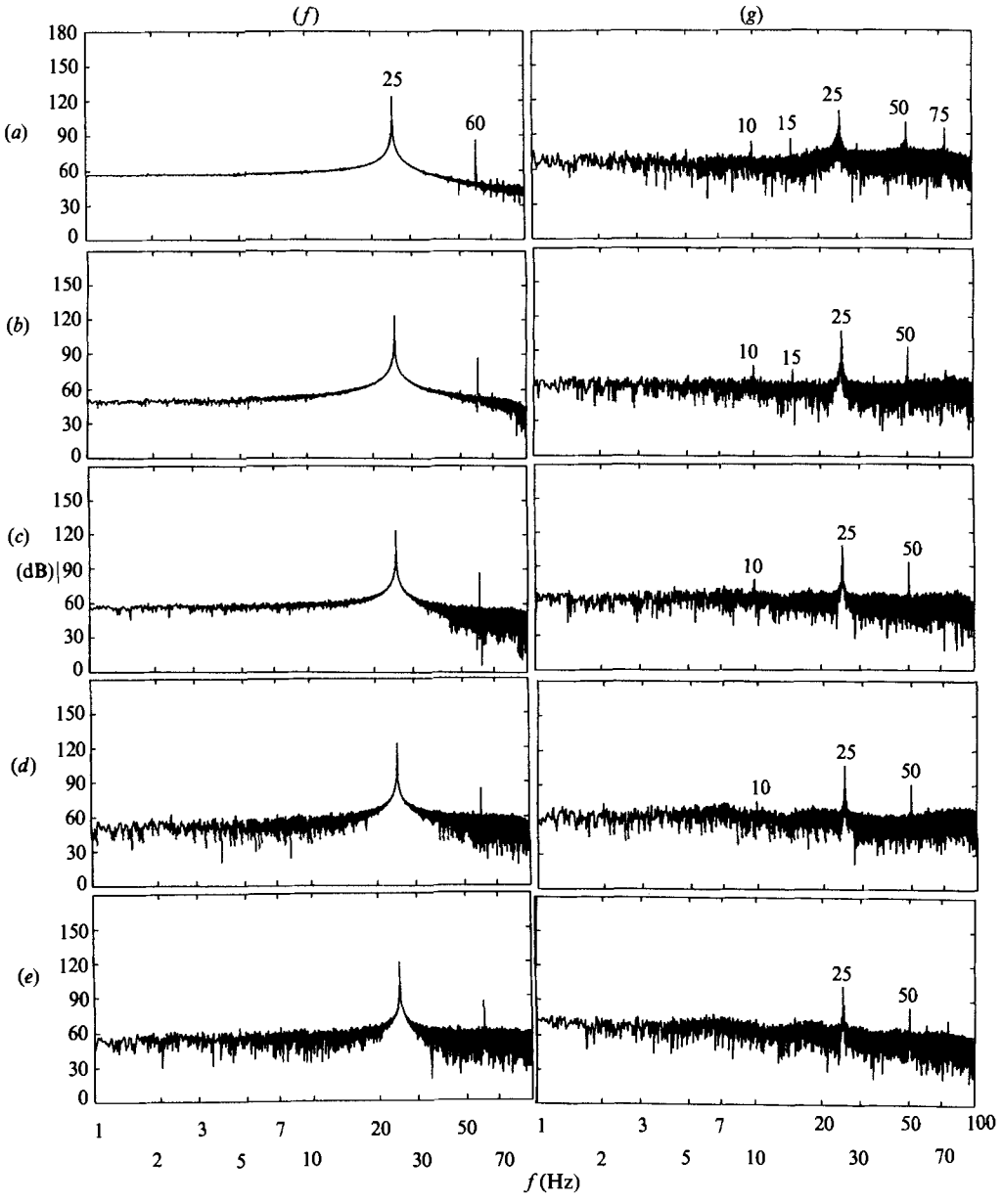

FIGURE 11. Amplitude–frequency spectra for a 25 Hz test wavetrain ($\mathscr{A} = 1.2$ V) in the presence of random background waves; $h = 5$ cm, $T = 73$ dyn/cm. Row (*a*) no random waves; row (*b*) SNR = 40 dB; row (*c*) SNR = 30 dB; row (*d*) SNR = 25 dB; row (*e*) SNR = 20 dB; column (*f*) command signal; column (*g*) wave-gauge signal at $(x, y) = (7, -4.7)$ cm.

As discussed earlier, the spectral amplitude of a discrete component in B_h must exceed a threshold amplitude above the surrounding noise levels in order to cause selective amplification. Rather than decrease the amplitude of the noise wavetrain relative to the natural background waves in the channel, as was illustrated by the results of figure 3, it is also instructive to generate pseudo-random waves directly, and increase their amplitude relative to the noise wavetrain. This was accomplished with a command signal containing a 25 Hz signal ($\mathscr{A}_{25} = 1.2$ V), a 60 Hz signal

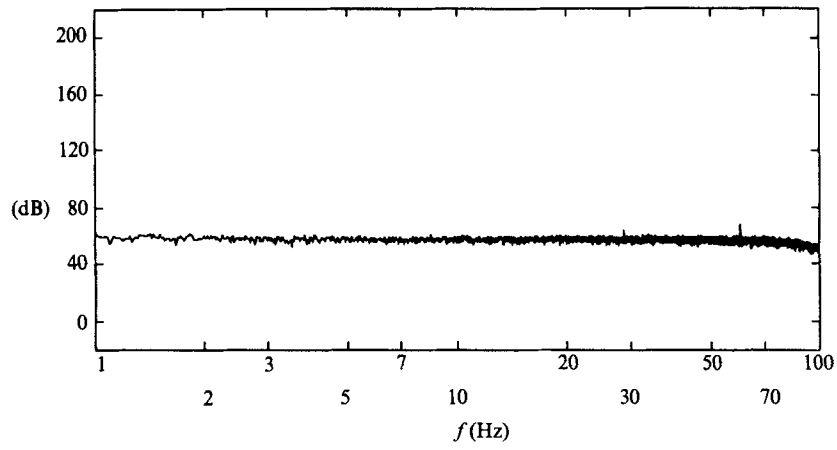

FIGURE 12. Averaged amplitude–frequency spectrum of naturally occurring background waves $\langle \mathscr{B} \rangle$ in the wave channel; wave gauge at $(x, y) = (7, -4.7)$ cm.

($\mathscr{A}_{60} = 0.01$ V), and 'white' noise at a specified signal-to-noise ratio (SNR) defined as

$$\text{SNR} = \frac{\text{r.m.s. of test wavetrain signal}}{\text{r.m.s. of white noise signal}} \tag{5}$$

where r.m.s. is the root-mean-square of deviations of the time series from its mean value. The SNR of the 60 Hz wavetrain is about 125 (42 dB), which was held constant in these experiments. (Note that the wave vectors for all wavetrains input by the wavemaker were initially collinear; however, according to the results of Part 3, wavetrains with frequencies greater than 9.8 Hz are expected to spread directionally their energy.) Figure 11 shows frequency spectra for the command signals (column *f*) and wave-gauge records (column *g*) for a series of experiments in which the SNR of the random waves was varied from 100 (40 dB) in row (*b*) to 10 (20 dB) in row (*e*). The frequency spectra of row (*a*) resulted when no random waves were added. The wave spectrum of row (*a*) shows the selective amplification of 10 and 15 Hz wavetrains, as seen previously; both have comparable spectrum amplitudes. When random waves were added so that the SNR = 100 (40 dB) in row (*b*), which is comparable to that of the 60 Hz noise wavetrain, the background spectral level over the entire frequency band of 1–100 Hz is, surprisingly, slightly lowered. In addition, the spectral amplitudes of the 10 and 15 Hz peaks are reduced, as are the superharmonics of the test wavetrain. When the SNR of the random waves is decreased to 32 (30 dB) in row (*c*), the 15 Hz peak disappears, along with the 75 Hz superharmonic of the test wavetrain. The background spectral level over the entire frequency band of 1–100 Hz is slightly raised. As the SNR decreases further in rows (*d*) and (*e*), the 10 Hz peak gradually disappears and the spectrum becomes somewhat bimodal from 5 to 20 Hz, the span of B_f. No selective amplification is apparent in row (*e*) where the r.m.s. of the test wavetrain is ten times larger than that of the background waves.

3.2. *Broad-banded spectral noise*

In this section we examine nonlinear interactions between a test wavetrain and background waves whose spectrum was broad-banded. The command signals to the

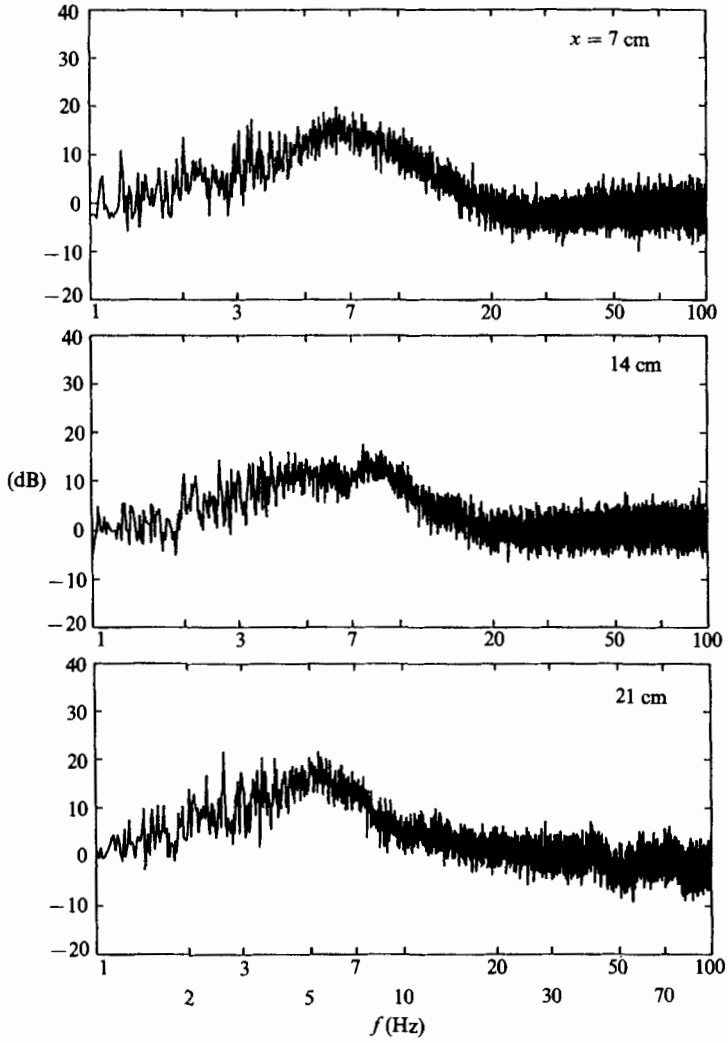

FIGURE 13. Evolution of averaged amplitude–frequency spectrum $\langle \mathscr{R} \rangle$ of the random waves down the wave channel.

wavemaker consisted of psuedo-random waves (white noise) plus a 25 Hz wave, i.e. no discrete noise components were added. The signal-to-noise ratio (SNR) was fixed at 10 (20 dB) and the command signal amplitude of the 25 Hz wavetrain was 1.2 V. Since only the statistical properties of the white noise were controlled, ensemble averages of 16 independent records are used to smooth the final results.

Experiments were conducted in the following manner. First, 16 time series of wave-gauge data were obtained sequentially, and frequency spectra were computed for the natural background noise in the tank when the wavemaker was powered, but not moving. These 16 frequency spectra were averaged to obtain a representative spectrum for the natural background noise, $\langle \mathscr{B} \rangle$, in the tank. Then 16 experiments were conducted using white-noise command signals to the wavemaker. Wave-gauge data were obtained and analysed for each experiment and an average frequency spectrum for the random waves in the presence of the tank's natural background

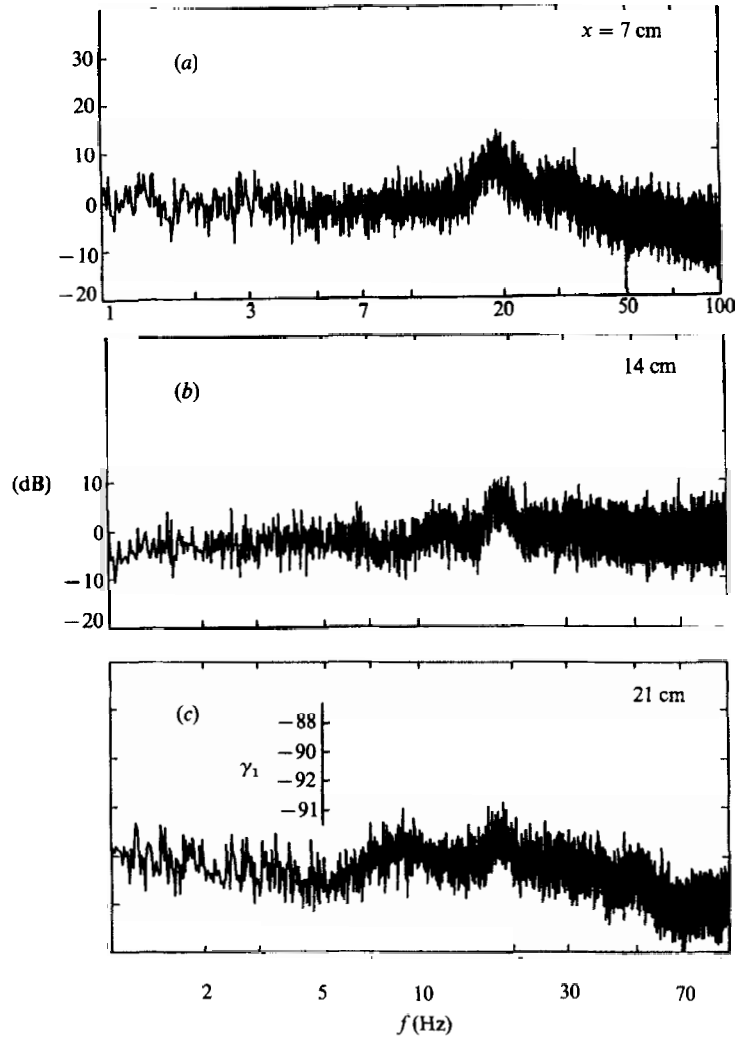

FIGURE 14. Evolution of averaged amplitude-frequency spectrum $\langle \mathscr{N} \rangle$, which shows the effects of nonlinear interactions, down the channel; $h = 5$ cm, $T = 73$ dyn/cm. Inset shows theoretical interaction coefficients.

noise, $\langle \mathscr{R} + \mathscr{B} \rangle$, was computed. Then 16 experiments were performed with the 25 Hz wavetrain (only) to find an averge frequency spectrum for the test wavetrain in the presence of the tank's natural background noise, $\langle \mathscr{T} + \mathscr{B} \rangle$. The test-wavetrain signal was then added to the 16 command signals of white noise and 16 more experiments were conducted and analysed to find an average frequency spectrum for the test wavetrain with random waves and the tank's background noise, $\langle \mathscr{T} + \mathscr{R} + \mathscr{B} \rangle$. These four average spectra were then combined linearly to find the average frequency spectrum for the random waves alone, i.e. $\langle \mathscr{R} \rangle = \langle \mathscr{R} + \mathscr{B} \rangle - \langle \mathscr{B} \rangle$, the test wavetrain alone, i.e. $\langle \mathscr{T} \rangle = \langle \mathscr{T} + \mathscr{B} \rangle - \langle \mathscr{B} \rangle$, and to display the effects of nonlinear interactions by calculating

$$\langle \mathscr{N} \rangle := \langle \mathscr{T} + \mathscr{R} + \mathscr{B} \rangle - \langle \mathscr{T} \rangle - \langle \mathscr{R} \rangle - \langle \mathscr{B} \rangle; \tag{6}$$

hence, $\langle \mathscr{N} \rangle$ is null if nonlinear interactions are insignificant. (We tacitly assume that the natural background noise in the tank is sufficiently small to interact linearly with

the random and test wavetrains.) The series of experiments and calculations outlined above were performed at three gauge sites downstream of the wavemaker. In addition to wave-gauge data, we also analysed the command and wavemaker feedback signals; all these time series required the collection and analysis of 50 mB of data at each gauge site.

Figure 12 shows the ensemble-averaged frequency spectrum for the natural background noise $\langle \mathscr{B} \rangle$ in the tank obtained at $(x, y) = (7, -4.7)$ cm. (This result is typical of background noise measurements at all gauge positions.) The amplitudes of background noise are distributed smoothly and fairly uniformly over the frequency band 1–100 Hz. (The spectral peak at 60 Hz is the ubiquitous electronic noise.) Figure 13 shows the ensemble-averaged frequency spectra of the random wavetrains $\langle \mathscr{R} \rangle$ at three downstream positions. At the first measurement site, $x = 7$ cm, the spectral amplitudes begin increasing near 2 Hz, reach a maximum of about 16 dB near 7 Hz, and decrease thereafter with negligible amplitudes above 20 Hz. At $x =$ 14 cm, the random waves are still confined to the frequency band 2–20 Hz; however, amplitudes are more uniformly distributed with a 12 dB maximum. At the last measurement site ($x = 21$ cm), a general downshift in amplitudes has occurred with a maximum of 16 dB at about 5 Hz; presumably, this downshift is a consequence of viscous damping, which increases with wave frequency.

The main results of these experiments are presented in figure 14 where the ensemble-averaged spectra $\langle \mathscr{N} \rangle$ are shown for three downstream measurement stations. Note that $\langle \mathscr{N} \rangle$ is not null, indicating that significant nonlinear interactions occurred. At the first measurement station ($x = 7$ cm), wave amplitudes in a frequency band 16–22 Hz increased with a maximum amplification of 8 dB at 19 Hz. Note that most of this frequency band lies in the low-frequency continuum B_ℓ for the 25 Hz test wavetrain. Wave amplitudes in the high-frequency continuum B_h decreased, down 8 dB near 100 Hz. At $x = 14$ cm wave amplitudes in the frequency band 1–7 Hz decreased by about 4 dB. In the range of 7–22 Hz, wave amplitudes increased in a bimodal manner with maxima near 12 and 19 Hz and a minimum near 15 Hz. Beyond 22 Hz, wave amplitudes at $x = 14$ cm show no amplification or attenuation; hence, the waves in B_h actually amplified since propagating from $x =$ 7 cm. At the last measurement site ($x = 21$ cm), wave amplitudes from 1–6 Hz remained lowered while wave amplitudes in B_h decreased again. The waves in B_ℓ remained amplified with the bimodal distribution observed at the previous station. This distribution is remarkably similar to the variation of the dynamical interaction coefficient γ_1 (Part 1 and the Appendix) over B_ℓ for the 25 Hz wavetrain; see the inset to figure 14(*c*). (A similar variation appears in row (*e*), column (*g*) of figure 11.) Hence, all waves in the low-frequency continuum are amplified in accordance with predictions of RIT for single triads when the background noise spectrum is broad-banded, i.e. there are no discrete components that cause selective amplification. None of the waves in the high-frequency continuum are amplified, also in accordance with the predictions of RIT for a single triad. However, the energy of waves in B_h does appear to cycle (down and back) during propagation, similar to the behaviour observed in the numerical computations of the Appendix.

4. Summary and conclusions

The evolution of ripple wavetrains generated mechanically in a channel was studied in the presence of different types of background waves (noise). Frequencies of the test wavetrains exceeded 19.6 Hz so that resonant triad interactions were

possible. Two types of background noise spectra were used: spectra that had discrete components and spectra that were broad-banded. Amplitude–frequency spectra were computed using measurements of *in situ* wave gauges; two-dimensional amplitude–wavenumber spectra were computed using spatial data obtained by remote sensing of the water surface with a high-speed imaging system. These data allowed definitive tests that established the existence of resonant triads in the experiments.

Experiments using noise with discrete spectral components in the high-frequency continuum, B_{h}, of allowable resonant triads for a test wavetrain showed that two waves in the low-frequency continuum, B_{ℓ}, of allowable triads could be selectively amplified – even when the SNR (signal-to-noise ratio based on amplitudes) was as large as 200. Selective amplification was not expected since the interaction coefficients for a resonant triad vary smoothly with frequency in B_{ℓ}. (Waves in B_{h} did not amplify, in accordance with expectations based on RIT.) It was conjectured that selective amplification resulted from a sequence of higher-order interactions that allowed the small amount of energy in the noise wavetrain to cascade to two waves in B_{ℓ}. In the conjectured scenario, a Benjamin–Feir-type instability, observed experimentally herein and described more thoroughly in Part 3, played an essential role. This instability allowed wavetrains with frequencies greater than 9.8 Hz to directionally spread their energy. The scenario for selective amplification is the following. First, the test and noise wavetrains become unstable according to the directional instability. They are now properly directed to excite a resonant triad with a wavetrain at their difference frequencies. The difference and noise wavetrains cannot be amplified by the test wavetrain in accordance with Hasselmann's theorem; however, they can exchange energy with each other. The difference wavetrain then becomes properly directed through the directional instability to excite a resonant triad with the test wavetrain and a new difference wavetrain. This process repeats until two difference wavetrains with frequencies in B_{ℓ} are excited that form a resonant triad with the test wavetrain. These two waves can be amplified by the test wavetrain, and their subsequent growth dominates all other resonant triad interactions. At each step in this sequence, there is a spatial distribution of resonant triads. If the difference wavetrain between the two waves in B_{ℓ} also lies in the low-frequency continuum, higher-order triads can result. This scenario comprises exceedingly small, higher-order interactions, normally ignored in RIT. Yet, it correctly predicts the observed frequencies in all of the experiments of Part 1, and all of the experiments presented herein.

When the background noise spectrum is broad-banded, no waves in B_{ℓ} are selectively amplified. Instead, all of the waves in this frequency band grow in accordance with the interaction coefficient for the test wavetrain. Waves in the high-frequency band do not amplify; however, there is experimental and numerical evidence that they cycle their energy during propagation. Both types of behaviour are in accordance with predictions of resonant interaction theory for a single triad.

In one experiment herein, a sideband (degenerate) resonant quartet was selectively amplified by a high-frequency background wave. Additional preliminary experiments show that (non-degenerate) resonant quartets are selectively amplified by a high-frequency background wave when the test wavetrain has a frequency of less than 19.6 Hz. (Resonant triads cannot occur for test wavetrains in this frequency range.) We shall report a comprehensive set of experimental data and discuss selective amplification of resonant quartets by noise spectra with discrete components in a subsequent paper.

Joe Hammack expresses sincere gratitude to John Miles for enabling a sabbatical visit to the Institute of Geophysics and Planetary Physics, UCSD, during which this manuscript was prepared. We are grateful to Harvey Segur for many helpful comments. Financial support, provided by the Army Research Office and the Office of Naval Research through the DoD University Research Instrumentation Program (grant number N00014-86-G-0201 with the University of Florida), is gratefully acknowledged. The equipment purchased under this contract was essential in performing this research. The College of Engineering at the University of Florida has made significant contributions to the development of the research laboratory, and that support is gratefully acknowledged. J. H. and M. P. also wish to thank the Office of Naval Research for their continuing support under contract N00014-85-K-0201 at the University of Florida. D. H. acknowledges financial support from the Office of Naval Research under contract N00014-84-K-0137 DARPA University Research Initiative (Contract N00014-K-0758) and an ARCS Fellowship at the University of California, San Diego.

Appendix. Numerical solutions of the three-wave equations

This section presents numerical solutions of the evolution equations for a resonant triad of ripple wavetrains to demonstrate the consequences of noise spectra with discrete components on a test wavetrain. These numerical results are somewhat qualitative, since the equations examined do not include spatial variations or coupling among triads.

A.1. *Inviscid dynamics*

The evolution (three-wave) equations for any conservative, weakly nonlinear, time-dependent dynamical system are given by

$$\frac{\mathrm{d}A_i}{\mathrm{d}t} = i\gamma_i A_{i+1}^* A_i^*, \tag{A 1}$$

where the interaction coefficients for ripple wavetrains (Simmons 1969) are

$$\gamma_i = -\frac{k_i}{4\omega_i}\sum_{j=1}^{3}\omega_j\omega_{j+1}(1+\boldsymbol{e}_j\cdot\boldsymbol{e}_{j+1}), \tag{A 2}$$

$A_i(t)$ is the complex amplitude of the ith member of the triad, (*) indicates complex conjugate, $\boldsymbol{e}_j$ is the unit vector in the direction of the jth wave vector, j is interpreted as modulo 3, and the frequencies include a $+/-$ sign such that

$$|\omega_1| - |\omega_2| - |\omega_3| = 0. \tag{A 3}$$

To test the conjectured mechanism for selective amplification, we numerically solved (A 1)–(A 3) with initial conditions relevant to our experiments. The numerical scheme used was a fifth-order Taylor series expansion with a time step of 0.002 s. Differentiating (A 1) four times provides the higher-order derivatives for the expansion. The simulated experiment used a 25 Hz test wave in the presence of a small 60 Hz noise wavetrain. It was conjectured in §3.1.1 that these waves would interact to create a small 35 Hz difference wave and a (60, 35, 25) Hz resonant triad that would not amplify. The 35 Hz wavetrain would then create a (35, 10, 25)-resonant triad that would not amplify. The 10 Hz wavetrain would then create a (25, 15, 10) Hz resonant triad that would amplify. The first two triads in this

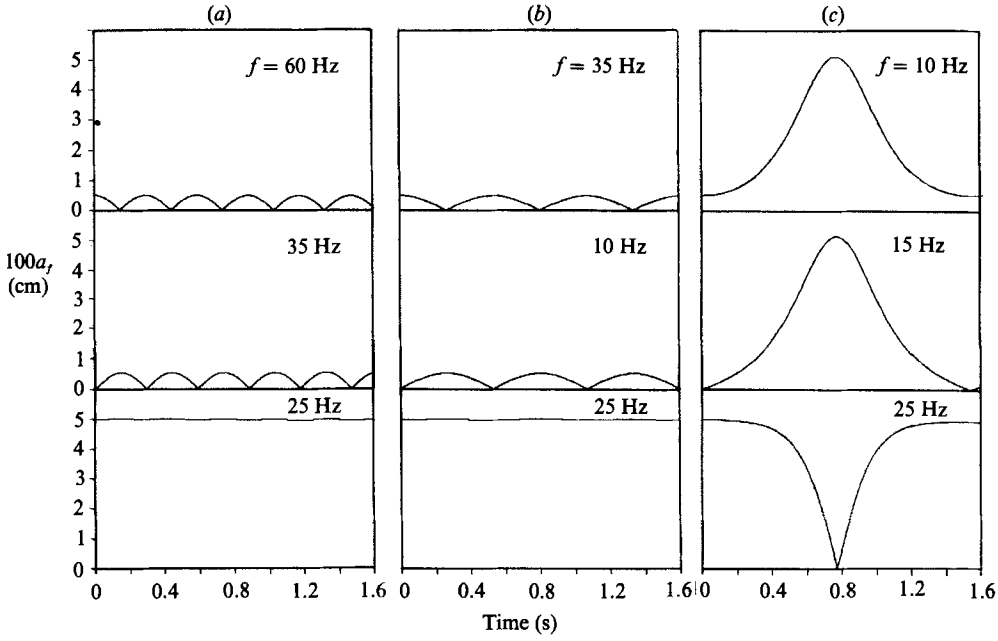

FIGURE 15. Numerical solutions of the inviscid three-wave equations showing the evolution of the (real) wave amplitude a_f for the following initial conditions on complex amplitude A_f: (*a*) $A_{60} = 0.004+0.003\mathrm{i}$ cm, $A_{35} = 0$, $A_{25} = 0.04+0.03\mathrm{i}$ cm; (*b*) $A_{35} = 0.004+0.003\mathrm{i}$ cm, $A_{10} = 0$, $A_{25} = 0.04+0.03\mathrm{i}$ cm; (*c*) $A_{10} = 0.004+0.003\mathrm{i}$ cm, $A_{15} = 0$, $A_{25} = 0.04+0.03\mathrm{i}$ cm.

scenario should not amplify, in accordance with Hasselmann's (1967) theorem. According to this theorem, which is based on linear stability analysis, when two waves in a resonant triad are small relative to the third, then the dominant wave must have the highest frequency in order to amplify the smaller waves. Hence, the (25, 15, 10) Hz triad in our scenario is the first that could amplify.

Figure 15 shows the numerical solutions of (A 1)–(A 3) for the 25 Hz wavetrain with a 60 Hz noise wavetrain. Column (*a*) corresponds to the initial triad interaction among the 60 Hz wavetrain, the 25 Hz test wavetrain, and their difference wavetrain. Here, the 25 Hz wavetrain has an initial amplitude that is ten times that of the 60 Hz wavetrain. The initial amplitude of the 35 Hz difference wavetrain is zero. During evolution, the 35 Hz wavetrain is created, receiving energy from the highest-frequency wavetrain (60 Hz). According to the linear stability analysis by Hasselmann, both small waves remain neutrally stable at their initial values. Hence, the 35 Hz wavetrain would not be created without nonlinearity, which allows the wave to grow but not to amplify beyond the initial amplitude of the highest-frequency wave. Since the 35 Hz wavetrain now has non-zero amplitude, it creates the (35, 10, 25) Hz resonant triad shown in column (*b*). Again, the 10 Hz difference wavetrain never grows larger than the highest-frequency wavetrain (35 Hz). The 10 Hz wavetrain then creates the (10, 15, 25) Hz resonant triad presented in column (*c*). A triad now exists in which the highest-frequency member has the most energy, and the lower-frequency members have frequencies in B_ℓ; hence, these two waves in B_ℓ are amplified, as shown.

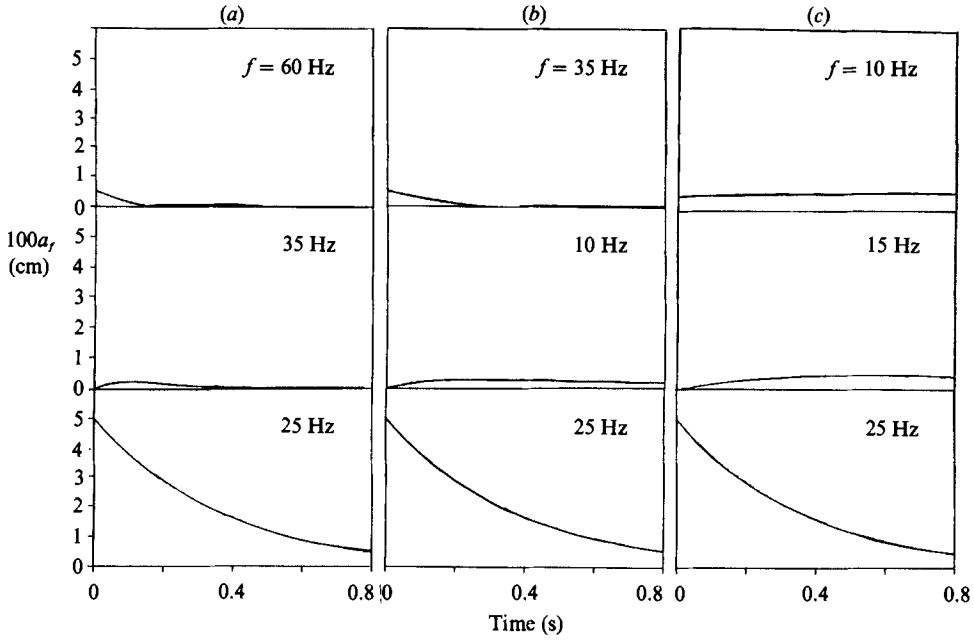

FIGURE 16. Numerical solutions of the viscous three-wave equations showing the evolution of the (real) wave amplitude a_f for the following initial conditions on complex amplitude A_f: (*a*) $A_{60} = 0.004+0.003\mathrm{i}$ cm, $A_{35} = 0$, $A_{25} = 0.04+0.03\mathrm{i}$ cm; (*b*) $A_{35} = 0.004+0.003\mathrm{i}$ cm, $A_{10} = 0$, $A_{25} = 0.04+0.03\mathrm{i}$ cm; (*c*) $A_{10} = 0.004+0.003\mathrm{i}$ cm, $A_{15} = 0$, $A_{25} = 0.04+0.03\mathrm{i}$ cm.

A.2. *Viscous dynamics*

Linear viscous damping is included in (A 1) by replacing

$$\frac{\mathrm{d}}{\mathrm{d}t} \rightarrow \frac{\mathrm{d}}{\mathrm{d}t} + \delta_i, \tag{A 4}$$

where δ_i is the linear decay rate. Henderson & Lee (1986) found that the decay of wavetrains studied using the present facility and procedures is accurately predicted by the model for an inextensible surface (Lamb 1932, p. 631), i.e.

$$\delta_i = \tfrac{1}{2} k_i (\tfrac{1}{2}\nu\omega_i)^{\frac{1}{2}}. \tag{A 5}$$

Numerical solutions of (A 1) with (A 4) and (A 5) are shown in figure 16 with the same initial conditions used in figure 15. In contrast to the inviscid calculations, viscosity causes the 60 Hz noise wavetrain in the triad of column (*a*) to decay rapidly. However, it survives long enough to excite the 35 Hz wavetrain, which then dies quickly owing to viscosity. Neither wavetrain is observable after about 0.4 s, or ten wavelengths of the 25 Hz wavetrain. In the triad of column (*b*) the 35 Hz wavetrain dies rapidly to viscosity, but first allows the 10 Hz difference wavetrain to be excited. The 10 Hz wavetrain survives the 35 Hz wavetrain, since it has a smaller decay rate; however, it has already begun to decay at 0.2 s (five wavelengths of the 25 Hz wavetrain). In addition the 10 Hz wavetrain never obtains an amplitude as large as the initial amplitude of the 35 Hz wavetrain. In the triad of column (*c*) the background wavetrains have frequencies in B_f; hence, the 15 Hz difference wavetrain, whose amplitude is zero initially, does grow as large as the initial

amplitude of the 10 Hz wavetrain. Neither the 10 Hz nor the 15 Hz background wavetrains have begun to decay significantly after 0.8 s (twenty wavelengths of the 25 Hz wavetrain). Additional computations show that the initial amplitude of the 60 Hz noise wavetrain must be at least $\frac{1}{70}$ of the test wavetrain in order for an observable 35 Hz difference wavetrain to be excited.

REFERENCES

CRAIK, A. D. D. 1985 *Wave Interactions and Fluid Flows.* Cambridge University Press.

FLICK, R. E. & GUZA, R. T. 1980 Paddle generated waves in laboratory channels. *J. Waterway, Port, Coastal, Ocean Div. ASCE* **106** (WW1), 79–97.

HASSELMANN, K. 1967 A criterion for nonlinear wave stability. *J. Fluid Mech.* **30**, 737–739.

HENDERSON, D. & HAMMACK, J. 1987 Experiments on ripple instabilities. Part 1. Resonant triads. *J. Fluid Mech.* **184**, 15–41.

HENDERSON, D. & LEE, R. 1986 Laboratory generation and propagation of ripples. *Phys. Fluids* **29**, 619–624.

LAMB, H. L. 1932 *Hydrodynamics.* Dover.

MCGOLDRICK, L. F. 1965 Resonant interactions among capillary-gravity waves. *J. Fluid Mech.* **21**, 305–331.

PERLIN, M. & HAMMACK, J. 1990 Experiments on ripple instabilities. Part 3. Resonant quartets of the Benjamin–Feir type (in preparation).

SIMMONS, W. F. 1969 A variational method for weak resonant wave interactions. *Proc. R. Soc. Lond.* A **309**, 551–571.

WILTON, J. R. 1915 On ripples. *Phil. Mag.* **29** (6), 688–700.